Journal of Molecular Modeling (2026) 32:315
https://doi.org/10.1007/s00894-026-06879-1

RESEARCH

Conjugated planar polymers and tubular nanobelts of the perfect in-plane [55555] metallo-annulene Pt©$C_{15}H_{10}$

Xiao-Ni Zhao[1,2] · Qin-Wei Zhang[1] · Qiang Chen[1] · Si-Dian Li[1]

Received: 15 April 2026 / Accepted: 1 August 2026

Abstract

Context Using the newly reported perfect in-plane [55555] metallo-annulene D_{5h} Pt©$C_{15}H_{10}$ (**1**) (Zhao et al., *Eur. J. Inorg. Chem.* 2025, 28, e202500420) as building blocks via partial dehydrogenations and based on extensive density functional theory calculations, we predict herein their stable conjugated planar polymers (Pt©C_{15})$_n$$H_{6n+4}$ (n = 2–9) (**2–9**) and (Pt©$C_{15}H_6$)$_{10}$ (**10**), non-metal sandwich complexes C_2(Pt©$C_{15}H_{10}$)$_2$ (**1′**), [C_2(Pt©C_{15})$_2$]$_n$$H_{2(6n+4)}$ (n = 2–9) (**2′-9′**), and [C_2(Pt©$C_{15}H_6$)$_2$]$_{10}$ (**10′**), and tubular nanobelts (Pt©$C_{15}H_6CH_2$)$_n$ (n = 8, 10, 12) (**11, 12, 13**). Detailed adaptive natural density partitioning (AdNDP) analyses indicate that the [55555] metallo-annulene polymers (Pt©C_{15})$_n$$H_{6n+4}$ (**2–9**) and (Pt©$C_{15}H_6$)$_{10}$ (**10**) consist of conjugated π-aromatic Pt©C_{15} building blocks interconnected by C_6 hexagonal units, non-metal bis([55555] metallo-annulene) sandwich complexes [C_2(Pt©C_{15})$_2$]$_n$$H_{2(6n+4)}$ (**2′-9′**) and [C_2(Pt©$C_{15}H_6$)$_2$]$_{10}$ (**10′**) contain n -C≡C- non-metal coordination centers each sandwiched between two aromatic Pt©C_{15} ligands, while the tubular [55555] metallo-annulene nanobelts (Pt©$C_{15}H_6CH_2$)$_n$ (**11, 12, 13**) possess n conjugated π-aromatic Pt©C_{15} building blocks interlinked by $n > CH_2$ carbene bridges. Bowl-shaped C_{5v} M©$C_{40}H_{15}$ (M = Au, Ag, Cu) (**14**) and their metal sandwich complexes D_{5h} Cr_5(M©$C_{40}H_{15}$)$_2$ (**14′**) are also proposed. The IR, Raman, and UV–vis spectra of the concerned species are theoretically simulated to facilitate their experimental characterizations.

Method All metallo-annulene structures were fully optimized at the B3LYP level using Gaussian 09, with SDD pseudopotentials/basis sets for the metals and 6-31G* basis set for C and H. Frequency analysis indicated that all structures as true minima. UV–Vis spectra were simulated via TD-DFT at B3LYP/def2-TZVP with the SMD solvent model (dichloromethane). BOMD simulations were performed using CP2K (GTH-PBE pseudopotentials, DZVP-MOLOPT-GTH basis sets), AdNDP bonding analyses were conducted and VMD and CYLview were used for structure and molecular orbital visualization.

Keywords First principles theory · Metallo-annulene · Conjugated Polymers · Nanobelt · Structure bonding

Introduction

The recent discovery of the osmium-centered in-plane [55555] metallo-annulene frameworks in 3D [Os]©$C_{15}H_{10}$ ([Os] = OsL^1L^2 and L stands for PPh_3, CO, or PEt_3 σ-ligands in axial direction) by Xia and co-workers in 2025 [1] represents a major breakthrough in organometallic chemistry. Such an in-plane coordination bonding pattern overcomes the structural limitations of traditional out-of-plane metallo-annulene complexes such as the well-known ferrocene Fe(η^5-C_5H_5)$_2$ [2] and bis(η^6-benzene) chromium Cr(η^6-C_6H_6)$_2$ [3] in which the metal centers are sandwiched between two aromatic annulene ligands. For over seven decades, the embedding of a metal center within the planar cavity of an annulene ring, which necessitates the formation of direct metal–carbon σ-bonds, had remained a fundamental challenge in chemistry. The syntheses and characterization of [Os]©$C_{15}H_{10}$ have redefined metalla-aromaticity [4]. In these complexes with two additional σ-ligands on the top and bottom of the Os atom to help stabilize the systems, the hepta-coordinate η^7-Os center is integrated into the [15] $C_{15}H_{10}$ annulene plane, with its d_{xz} and d_{yz} atomic orbitals participating in the overall delocalized π-conjugation of the

✉ Qiang Chen
chenqiang@sxu.edu.cn

✉ Si-Dian Li
lisidian@sxu.edu.cn

[1] Institute of Molecular Science, Shanxi University, Taiyuan 030006, China

[2] Department of Chemistry and Chemical Engineering, Jinzhong University, Jinzhong 030619, China

Published online: 14 August 2026

five pentagons over the [55555] metallo-annulene plane, rendering π-aromaticity and extra stability to the systems [1].

Based on extensive density functional theory (DFT) calculations and analyses, our group predicted late in 2025 a series of perfectly in-plane [55555] metallo-annulene complexes D_{5h} M©$C_{15}H_{10}$ (M = Pt, Pd, Ni) and D_{5h} M©$C_{15}H_{10}^{+}$ (M = Au, Ag, Cu) without the two extra σ-ligands needed [5]. The penta-coordinate transition metal center (η^5-M) matches the perfect planar [15]$C_{15}H_{10}$ annulene ligand both geometrically and electronically, forming overall nine delocalized π-bonds over the molecular plane conforming to the $4n+2$ Hückel's aromatic rule for closed-shell systems ($n=4$). The penta-coordinate η^5-M center in these aromatical complexes follows a distinctive $5\sigma+2\pi$ bonding pattern to help maintain the perfect planar structures of the systems. However, whether such stable in-plane [55555] metallo-annulene complexes can be extended in two or three dimensions to form more complicated in-plane [55555] metallo-annulene complexes with multiple η^5-M coordination centers or even low-dimensional nanomaterials still remains unknown in both experiments and theory.

Employing D_{5h} Pt©$C_{15}H_{10}$ (**1**) as building blocks via partial dehydrogenations, we predict in this study at DFT level a series of [55555] metallo-annulene polymers $(Pt©C_{15})_nH_{6n+4}$ ($n=2$–9) (**2**–**9**) and $(Pt©C_{15}H_6)_{10}$ (**10**), non-metal bis([55555] metallo-annulene) sandwich complexes $C_2(Pt©C_{15}H_{10})_2$ (**1′**), $[C_2(Pt©C_{15})_2]_nH_{2(6n+4)}$ ($n=2$–9) (**2′**-**9′**), and $[C_2(Pt©C_{15}H_6)_2]_{10}$ (**10′**), and tubular [55555] metallo-annulene nanobelts $(Pt©C_{15}H_6CH_2)_n$ ($n=8$, 10, 12) (**11, 12, 13**). Detailed Born–Oppenheimer molecular dynamic (BOMD) simulations, adaptive natural density partitioning (AdNDP) analyses, and IR, Raman, and UV–vis spectral simulations are performed on the concerned species to help comprehend their high-symmetry geometries and high stabilities and facilitate their future experimental syntheses and spectral characterizations.

Methods

The structures of metallo-annulenes were fully optimized at the hybrid B3LYP [6, 7] level using the Gaussian 09 package [8]. The SDD basis sets and related Stuttgart relativistic energy-consistent pseudopotentials were employed for Pt, Au, Ag, Cu, Cr, Mo and W atoms [9], while the standard 6-31G(d) [10, 11] basis sets were used for the C and H. Frequency analyses were performed at the same theoretical level to make sure that all the optimized structures are true minima of the systems without imaginary vibrational frequencies. Time-dependent density functional theory (TD-DFT) [12, 13] calculations were performed to simulate their UV–Vis spectra at B3LYP/def2-TZVP. In the TD-DFT calculations, the SMD model was used with dichloromethane as the solvent [14]. Detailed BOMD simulations were performed using the CP2K code with the GTH-PBE pseudopotentials and DZVP-MOLOPT-SR-GTH basis sets [15–17]. Detailed AdNDP bonding analyzes were performed on the concerned systems [18, 19]. Anisotropy of current-induced density (ACID) [20, 21] and gauge-including magnetically induced currents (GIMIC) [22] analyses were implemented on sandwich $C_2(Pt©C_{15}H_{10})_2$ (**1'**) to graphically display the ring currents induced by an external magnetic field in vertical direction perpendicular to the ligand planes. The VMD [23] and CYLview [24] programs were used for the visualization of structures and molecular orbitals.

Results and discussion

Structures and stabilities

Using the in-plane D_{5h} Pt©$C_{15}H_{10}$ (**1**)[5] as building blocks, Fig. 1 depicts the optimized structures of their planar or quasi-planar [55555] metallo-annulene polymers on the left column, including D_{2h} $(Pt©C_{15})_2H_{16}$ (**2**), C_{2v} $(Pt©C_{15})_3H_{22}$ (**3**), C_{2v} $(Pt©C_{15})_4H_{28}$ (**4**), C_{2v} $(Pt©C_{15})_5H_{34}$ (**5**), C_{2v} $(Pt©C_{15})_6H_{40}$ (**6**), C_{2v} $(Pt©C_{15})_7H_{46}$ (**7**), C_{2v} $(Pt©C_{15})_8H_{52}$ (**8**), and C_2 $(Pt©C_{15})_9H_{58}$ (**9**) in the general formula of $(Pt©C_{15})_nH_{6n+4}$ ($n=2$–9), and D_{10h} $(Pt©C_{15}H_6)_{10}$ (**10**) which can be generated via the following partial dehydrogenation reactions:

$$n\mathrm{Pt©C_{15}H_{10}} = \left(\mathrm{Pt©C_{15}}\right)_n\mathrm{H_{6n+4}} + 2(n-1)\mathrm{H_2} \quad (n = 2-9) \tag{1}$$

$$10\mathrm{Pt©C_{15}H_{10}} = \left(\mathrm{Pt©C_{15}H_6}\right)_{10} + 20\mathrm{H_2} \tag{2}$$

The planar D_{2h} $(Pt©C_{15})_2H_{16}$ (**2**) contains two equivalent Pt©C_{15} building blocks interconnected by one C_6 hexagonal unit between them via two C–C σ-bonds, while C_{2v} $(Pt©C_{15})_3H_{22}$ (**3**) consists of three Pt©C_{15} building blocks interlinked by two C_6 hexagons. Such situations exist in the whole $(Pt©C_{15})_nH_{6n+4}$ ($n=4$–9) (**4**–**9**) series which possess n Pt©C_{15} building blocks on the framework interconnected by $(n-1)$ C_6 hexagonal units between them. The perfect planar decagonal D_{10h} $(Pt©C_{15}H_6)_{10}$ (**10**) with the optimized ring radius of $r=11.62$ Å is composed of ten equivalent Pt©C_{15} building blocks in a circle interlinked by ten C_6 hexagons. Its D_{10h} symmetry displays a perfect combination of ten equivalent planar C_{2v} Pt©$C_{15}H_6$ structural units interlinked by ten C_{2v} C_6 hexagons. These [55555] metallo-annulene polymers all appear to be true minima on their potential energy surfaces, with the smallest vibrational frequencies ranging between $\nu_{min}=25.1$ cm^{-1} in D_{2h} $(Pt©C_{15})_2H_{16}$ (**2**), $\nu_{min}=3.3$ cm^{-1} in D_{10h} $(Pt©C_{15})_{10}H_{60}$ (**10**), and 1.1 cm^{-1} in C_2 $(Pt©C_{15})_9H_{58}$ (**9**). These planar

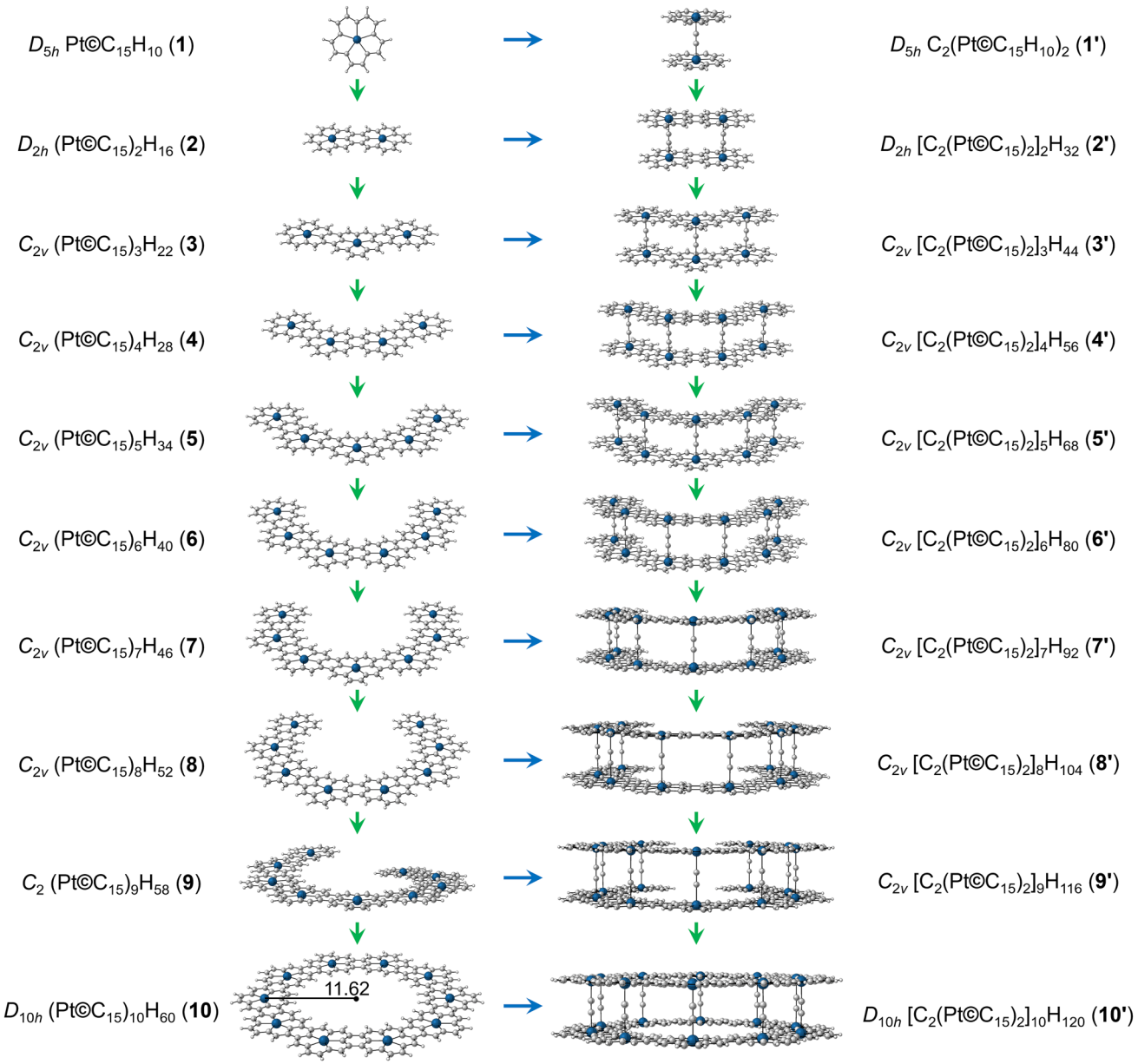

Fig. 1 Optimized structures of the [55555] metallo-annulene D_{5h} Pt©$C_{15}H_{10}$ (**1**) and its planar or quasi-planar polymers D_{2h} (Pt©C_{15})$_2H_{16}$ (**2**), C_{2v} (Pt©C_{15})$_3H_{22}$ (**3**), C_{2v} (Pt©C_{15})$_4H_{28}$ (**4**), C_{2v} (Pt©C_{15})$_5H_{34}$ (**5**), C_{2v} (Pt©C_{15})$_6H_{40}$ (**6**), C_{2v} (Pt©C_{15})$_7H_{46}$ (**7**), C_{2v} (Pt©C_{15})$_8H_{52}$ (**8**), C_2 (Pt©C_{15})$_9H_{58}$ (**9**), and D_{10h} (Pt©C_{15})$_{10}H_{60}$ (**10**) and their corresponding nonmetal bis([55555] metallo-annulene) sandwich complexes D_{5h} C_2(Pt©$C_{15}H_{10}$)$_2$ (**1'**), D_{2h} [C_2(Pt©C_{15})$_2$]$_2H_{32}$ (**2'**), C_{2v} [C_2(Pt©C_{15})$_2$]$_3H_{44}$ (**3'**), C_{2v} [C_2(Pt©C_{15})$_2$]$_4H_{56}$ (**4'**), C_{2v} [C_2(Pt©C_{15})$_2$]$_5H_{68}$ (**5'**), C_{2v} [C_2(Pt©C_{15})$_2$]$_6H_{80}$ (**6'**), C_{2v} [C_2(Pt©C_{15})$_2$]$_7H_{92}$ (**7'**), C_{2v} [C_2(Pt©C_{15})$_2$]$_8H_{104}$ (**8'**), C_{2v} [C_2(Pt©C_{15})$_2$]$_9H_{116}$ (**9'**), and D_{10h} [C_2(Pt©C_{15})$_2$]$_{10}H_{120}$ (**10'**) at B3LYP level, with the ring radius of D_{10h} (Pt©C_{15})$_{10}H_{60}$ (**10**) indicated in Å

or quasi-planar [55555] metallo-annulene polymers possess the relatively large calculated HOMO–LUMO energy gaps decreasing monocratically from $\Delta E_{gap} = 3.47$ eV in Pt©$C_{15}H_{10}$ (**1**), $\Delta E_{gap} = 2.19$ eV in (Pt©C_{15})$_2H_{16}$ (**2**), to $\Delta E_{gap} = 1.21$ eV in (Pt©$C_{15}H_6$)$_{10}$ (**10**) as tabulated in Table S1, suggesting their reduced electronic reactivity and high chemical stability. Reactions (1) and (2) possess the calculated negative Gibbs free energy changes of $\Delta G^\circ = -2.81$, -5.74, -8.19, -10.69, -13.19, -15.68, -18.26, -20.56, -30.28 kcal/mol for n = 2, 3, 4, 5, 6, 7, 8, 9, and 10 at 298 K, respectively, showing that the concerned species are all feasible in thermodynamics. Replacing the η^5-Pt centers in **2**–**10** with Pd, the corresponding (Pd©C_{15})$_n H_{6n+4}$ ($n = 2$–9) all appear to be true minima, while D_{10h} Pd©$C_{15}H_6$)$_{10}$ turns out to be a saddle point with multiple imaginary vibrational frequencies (Figure S1).

As shown in Fig. 1 in the right column, utilizing planar [55555] metallo-annulene polymers **1–10** as effective ligands to sandwich one to ten -C≡C- coordination centers, a series of stable non-metal bis([55555] metallo-annulene) sandwich complexes can be formed, including D_{5h} $C_2(Pt©C_{15}H_{10})_2$ (**1'**), D_{2h} $[C_2(Pt©C_{15})_2]_2H_{32}$ (**2'**), C_{2v} $[C_2(Pt©C_{15})_2]_3H_{44}$ (**3'**), C_{2v} $[C_2(Pt©C_{15})_2]_4H_{56}$ (**4'**), C_{2v} $[C_2(Pt©C_{15})_2]_5H_{68}$ (**5'**), C_{2v} $[C_2(Pt©C_{15})_2]_6H_{80}$ (**6'**), C_{2v} $[C_2(Pt©C_{15})_2]_7H_{92}$ (**7'**), C_{2v} $[C_2(Pt©C_{15})_2]_8H_{104}$ (**8'**), and C_{2v} $[C_2(Pt©C_{15})_2]_9H_{116}$ (**9'**) in the general formula of $[C_2(Pt©C_{15})_2]_nH_{2(6n+4)}$ ($n = 2$–9), and D_{10h} $[C_2(Pt©C_{15})_{10}H_{60}]_2$ (**10'**). These non-metal sandwich complexes are all true minima on the potential energy surfaces with the decreasing HOMO–LUMO gaps of $\Delta E_{gap} = 1.42$, 1.22, 1.13, 1.05, 0.98, 0.93, 0.90, 0.88, 0.86, and 0.78 eV, respectively. We notice that the [55555] metallo-annulene polymer ligands in their non-metal sandwich complexes **1'−10'** all become almost perfectly planar, including the two equivalent $(Pt©C_{15})_9H_{58}$ (**9**) ligands in C_{2v} $[C_2(Pt©C_{15})_2]_9H_{116}$ (**9'**) which originally has a C_2 helical structure (**9**) (Fig. 1).

Extensive BOMD simulations performed in Fig. 2 for 60 ps indicate that, with the small calculated average root-mean-square deviations of RMSD = 0.06, 0.04, 0.05 Å and maximum bond length deviations of MAXD = 0.19, 0.14, 0.16 Å for D_{2h} $(Pt©C_{15})_2H_{16}$ (**2**) at 500 K, D_{5h} $C_2(Pt©C_{15}H_{10})_2$ (**1'**) at 1000 K, and $[C_2(Pt©C_{15})_2H_{16}]_2$ (**2'**) at 500 K, respectively, these [55555] metallo-annulene polymers and their non-metal sandwich complexes all appear to be dynamically stable at high temperatures.

Furthermore, as shown in Fig. 3, with D_{5h} $Pt©C_{15}H_{10}$ (**1**) as building blocks, a series of high-symmetry tubular [55555] metallo-annulene nanobelts in the general formula of $(Pt©C_{15}H_6CH_2)_n$ ($n = 8$, 10, 12) can be formed via the partial dehydrogenation reaction of

$$n\mathrm{Pt©C_{15}H_{10}} + n\mathrm{CH_4} = \left(\mathrm{Pt©C_{15}H_6CH_2}\right)_n + 3n\mathrm{H_2} (n = 8, 10, 12) \quad (3)$$

including D_{4h} $(Pt©C_{15}H_6CH_2)_8$ (**11**), D_{5h} $(Pt©C_{15}H_6CH_2)_{10}$ (**12**), and D_{6h} $(Pt©C_{15}H_6CH_2)_{12}$ (**13**) which contain n equivalent $Pt©C_{15}H_6$ building blocks interlinked by $n > CH_2$ carbene units. As the first metallo-annulene nanobelts reported to date similar to the newly discovered triple stranded porphyrin nanobelts [25], $(Pt©C_{15}H_6CH_2)_8$ (**11**), $(Pt©C_{15}H_6CH_2)_{10}$ (**12**), and $(Pt©C_{15}H_6CH_2)_{12}$ (**13**) possess the calculated tube radii of $r = 9.67$, 12.12, and 14.85 Å and large HOMO–LUMO gaps of $\Delta E_{gap} = 2.09$, 2.10, 2.07 eV, respectively.

As indicated in Fig. 4(a), the previously reported π-aromatic planar D_{5h} $M©C_{15}H_{10}^+$ (M = Au, Ag, Cu) [5] can also been extended in two dimensions to form the neutral bowl-shaped metallo-annulenes C_{5v} $M©C_{40}H_{15}$ (M = Au, Ag, Cu) (**14**), with the M–C bond lengths changing from $r_{M\text{-}C} = 2.120$ Å, 2.234 Å, and 2.186 Å in D_{5h} $M©C_{15}H_{10}^+$ (M = Au, Ag, Cu) [5] to $r_{M\text{-}C} = 2.168$ Å, 2.188 Å, and 2.129 Å in C_{5v} $M©C_{40}H_{15}$ (M = Au, Ag, Cu) (**14**) (Figure S2), respectively. Their large calculated HOMO–LUMO energy gaps of $\Delta E_{gap} = 3.34$, 2.97, and 2.65 eV show the high chemical stabilities of these quasi-planar systems. The calculated small averaged RMSD values of 0.06, 0.07, and 0.07 Å

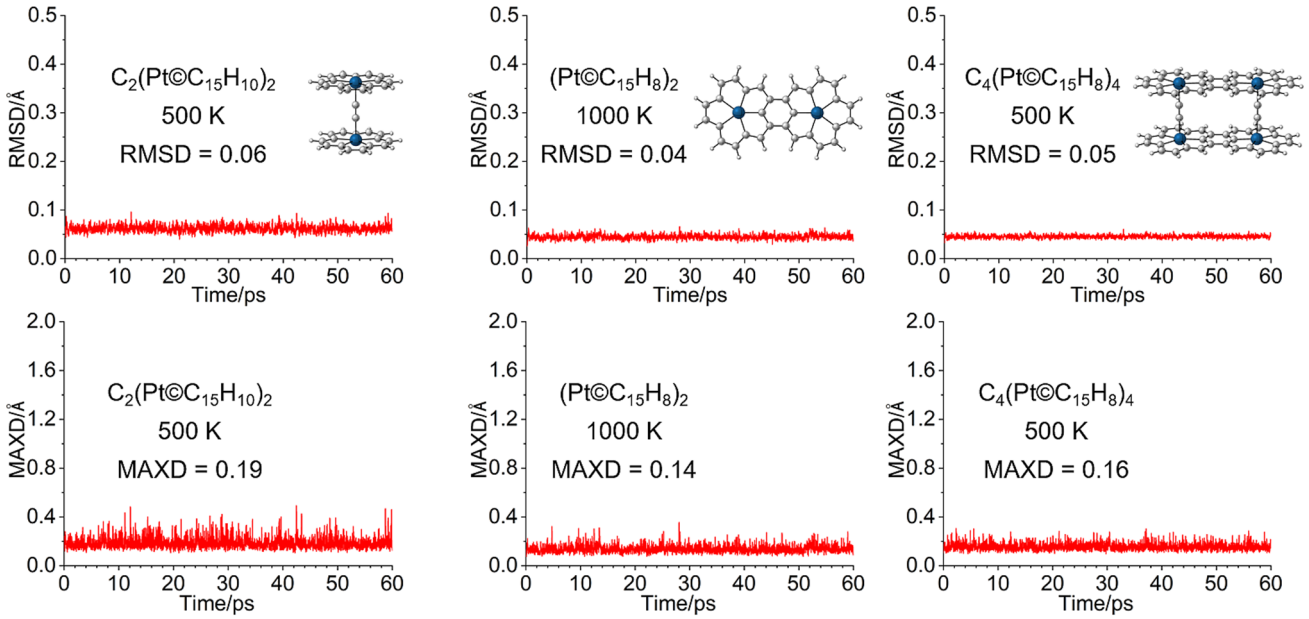

Fig. 2 BOMD simulations of D_{5h} $C_2(Pt©C_{15}H_{10})_2$ (**1'**) at 500 K and D_{2h} $(Pt©C_{15})_2H_{16}$ (**2**) at 500 K, and D_{2h} $[C_2(Pt©C_{15})_2]_2H_{32}$ (**2'**) at 500 K for 60 ps, with the corresponding RMSD and MAXD values indicated in Å

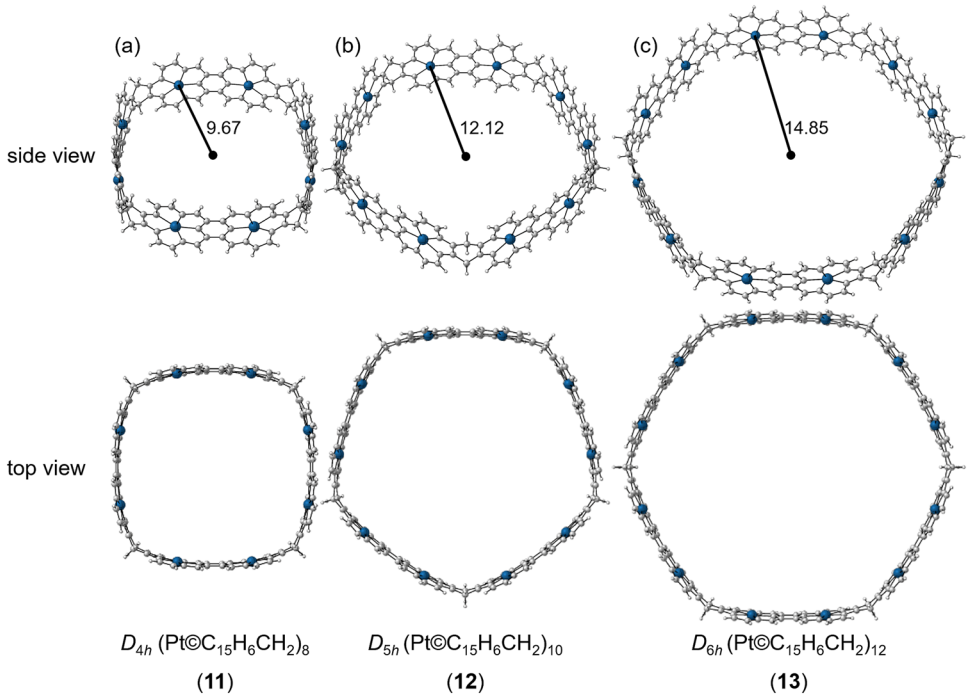

Fig. 3 Optimized structures of the tubular [55555] metallo-annulene nanobelts (**a**) D_{4h} (Pt©$C_{15}H_6CH_2)_8$ (**11**), (**b**) D_{5h} (Pt©$C_{15}H_6CH_2)_{10}$ (**12**), and (**c**) D_{6h} (Pt©$C_{15}H_6CH_2)_{12}$ (**13**), with the tubular radii indicated in Å

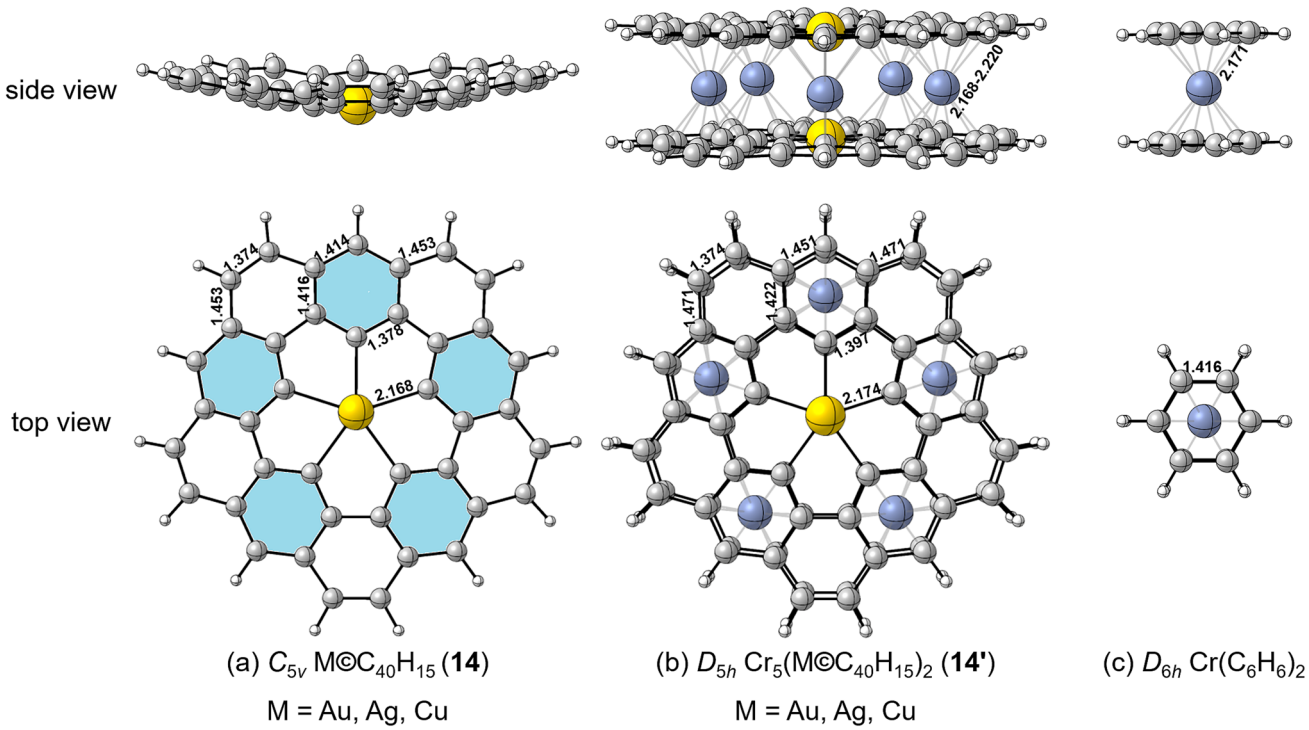

Fig. 4 Optimized structures of the (**a**) bowl-shaped C_{5v} M©$C_{40}H_{15}$ (M = Au, Ag, Cu) (**14**) and (**b**) the corresponding bis[55555] metallo-annulene sandwich complexes D_{5h} Cr_5(M©$C_{40}H_{15})_2$ (**14′**) at B3LYP, compared with that of (**c**) D_{6h} Cr($C_6H_6)_2$, with the necessary bond lengths indicated in Å for M = Au

and MAXD values of 0.20, 0.21, and 0.24 Å for M = Au, Ag, and Cu in the BOMD simulations at 1200 K for 60 ps in Figure S3 indicate that these bowl-shaped metallo-annnule complexes are all dynamically stable at high temperatures. Similar bowl-shaped metallo-annulene monoanions C_{5v} M©$C_{40}H_{15}^-$ (M = Pt, Pd) and D_{5h} Ni©$C_{40}H_{15}^-$ have also

been obtained (Figure S4). It is worth noticing that the C_{5v} M©$C_{40}H_{15}$ (M = Au, Ag, Cu) (**14**) metallo-annulene complexes contain five M-C σ-coordination bonds between the M coordination center and five equivalent C_6 hexagons highlighted in blue in Fig. 4a, indicating that each C_6 hexagon with 1 C-H σ-bond, 4 C–C σ-bonds, and 1 C-M σ-bond around it exhibits benzene-like behaviors. With the respiration in mind, we designed the high-symmetry metal-centered [55555] metallo-annulene sandwich complexes D_{5h} $Cr_5(M©C_{40}H_{15})_2$ (**14'**) (M = Au, Ag, Cu) which possess the decreasing HOMO–LUMO energy gaps of $\Delta E_{gap} = 2.33$, 1.85, and 1.50 eV, respectively, with each Cr atom sandwiched by two C_6 hexagons on the top and bottom, forming five local $Cr(C_6)_2$ sandwich structures analogous to bis(benzene) chromium $Cr(C_6H_6)_2$ (Fig. 4c). The optimized Cr–C coordination bond lengths between 2.168–2.220 Å in these local $Cr(C_6)_2$ sandwich structures well match the corresponding Cr–C distance of 2.171 Å in D_{6h} $Cr(C_6H_6)_2$, strongly supporting the observation that $Cr_5(Au©C_{40}H_{15})_2$ (**14'**) possesses five local $Cr(C_6)_2$ sandwich structures analogous to $Cr(C_6H_6)_2$. D_{5h} $Cr_5(M©C_{40}H_{15})_2$ (**14'**) thus represents the first annulene sandwich complex which possess both in-plane η^5-M (M = Au, Ag, Cu) and out-of-plane η^{12}-Cr transition-metal coordination centers, as shown in Fig. 4 and Figure S5. Similar results have also been obtained for $Mo_5(M©C_{40}H_{15})_2$ and $W_5(M©C_{40}H_{15})_2$ (M = Au, Ag, Cu), as shown in Figure S6. BOMD simulations performed in Figure S7 suggest that D_{5h} $Cr_5(M©C_{40}H_{15})_2$ (**14'**) (M = Au, Ag, Cu) are dynamically stable at 1000 K.

Bonding pattern analyses

As demonstrations, detailed AdNDP bonding pattern analyses are performed on the high-symmetry perfect planar [55555] metallo-annulene polymer D_{10h} $(Pt©C_{15})_{10}H_{60}$ (**10**) and non-metal bis([55555] metallo-annulene) sandwich complex D_{5h} $C_2(Pt©C_{15}H_{10})_2$ (**1'**) in Fig. 5. As shown in Fig. 5a that, in addition to the 60 2c-2e C-H σ-bonds and 170 2c-2e C–C σ-bonds with the occupation number of ON = 1.97–1.99 |e| in the first row on the ligand framework, each η^5-Pt center in D_{10h} $(Pt©C_{15})_{10}H_{60}$ (**10**) in the second row possesses 1 $5d_{z2}$ lone pair with ON = 1.99 |e| and forms 5 2c-2e Pt-C σ bonds with its five closest C neighbors with ON = 1.96 |e|, both its $5d_{xz}$ and $5d_{yz}$ orbitals participate in 2 6c-2e delocalized π-bonds with the five pentagons around it as well with ON = 1.99 |e|. Each η^5-Pt center in $(Pt©C_{15})_{10}H_{60}$ (**10**) thus follows the same $5\sigma + 2\pi$ coordination bonding pattern as that of the η^5-Pt center in D_{5h} $Pt©C_{15}H_{10}$ (**1**) [5]. It is also noticed that, as expected, each C_{2v} $Pt©C_{15}H_6$ unit in $(Pt©C_{15})_{10}H_{60}$ (**10**) possesses 7 15c-2e delocalized π-bonds with ON = 1.80–1.99 |e| in the third row, in the same bonding pattern as that in an isolated D_{5h} $Pt©C_{15}H_{10}$ (**1**) [5]. Thus, each C_{2v} $Pt©C_{15}H_6$ unit in $(Pt©C_{15})_{10}H_{60}$ (**10**) possesses overall nine delocalized π-bonds over its planar framework matching the Huckel's 4n + 2 rule, making it locally π-aromatic in nature. We conclude that D_{10h} $(Pt©C_{15})_{10}H_{60}$ (**10**) consists of ten equivalent conjugated π-aromatic C_{2v} $Pt©C_{15}H_6$ units on its perfectly planar circular molecular framework. The other eight [55555] metallo-annulene polymers $(Pt©C_{15})_nH_{6n+4}$ ($n = 2$–9) (**2–9**) with lower symmetries follow similar overall bonding patterns, as demonstrated in the case of D_{2h} $(Pt©C_{15})_2H_{16}$ (**2**) in Figure S8. We also performed bonding analyses on the tubular nanobelt D_{nh} $(Pt©C_{15}H_6CH_2)_n$ (**11**, **12**, **13**), as demonstrated in the case of D_{4h} $(Pt©C_{15}H_6CH_2)_8$ (**11**) in Figure S9. The results indicate that the η^5-Pt centers in these nanobelts follow the same $5\sigma + 2\pi$ coordination bonding pattern as that of the Pt center in $Pt©C_{15}H_{10}$ (**1**) [5].

Figure 5b indicates that the bonding pattern of the non-mental bis([55555] metallo-annulene) sandwich complex D_{5h} $C_2(Pt©C_{15}H_{10})_2$ (**1'**) also appears to be intriguing. The non-metal -C≡C- coordination center possesses 2 2c-2e π-bonds and 1 2c-2e σ-bond on the C≡C dumbbell, it also participates in 2 2c-2e Pt-C σ-bonds and 1 4c-2e Pt-C_2-Pt σ-bond which link the two $Pt©C_{15}H_{10}$ ligands together, while the two $Pt©C_{15}H_{10}$ ligands on the top and bottom possess 2 6c-2e delocalized π-bonds and 7 15c-2e delocalized π-bonds each over the ligand plane, making them locally π-aromatic in nature. Detailed ACID and GIMIC analyses of the sandwich D_{5h} $C_2(Pt©C_{15}H_{10})_2$ (**1'**) in Figure S10 clearly show the existence of clockwise ring currents induced by an external magnetic field along the C_5 molecular axis, further evidencing the local aromaticity of the two identical $Pt©C_{15}H_{10}$ ligands in the complex. The non-mental -C≡C- center sandwiched between two aromatic $Pt©C_{15}H_{10}$ ligands thus follows an out-of-plane coordination bonding pattern in D_{5h} $C_2(Pt©C_{15}H_{10})_2$ (**1'**), similar to the situation in the traditional out-of-plane transition metal sandwich complexes such as D_{6h} $Cr(C_6H_6)_2$ and D_{5h} $Fe(C_5H_5)_2$. In such a coordination bonding pattern, each C atom in the -C≡C- coordination center in $C_2(Pt©C_{15}H_{10})_2$ (**1'**) carries the calculated negative net atomic charge of $q_C = -0.23$ |e|, while the two equivalent Pt coordination centers possess the positive atomic charge of $q_{Pt} = +0.33$ |e| each. Similar bonding patterns and charge distributions exist in $[C_2(Pt©C_{15})_2]_nH_{2(6n+4)}$ ($n = 2$–9) (**2′-9′**) and $[C_2(Pt©C_{15}H_6)_2]_{10}$ (**10′**). As indicated in Figure S11, the in-plane η^5-Au center in the bowl-shaped C_{5v} $Au©C_{40}H_{15}$ (**14**) follows the same $5\sigma + 2\pi$ coordination bonding pattern as that of the η^5-Au in D_{5h} $Au©C_{15}H_{10}^+$ [5], while its metallo-annulene sandwich complex D_{5h} $Cr_5(Au©C_{40}H_{15})_2$ (**14′**) possesses five equivalent out-of-plane Cr coordination centers matching the 18-eletron rule, in the same coordination bonding pattern as that of the Cr center in D_{6h} $Cr(C_6H_6)_2$ (Figure S12).

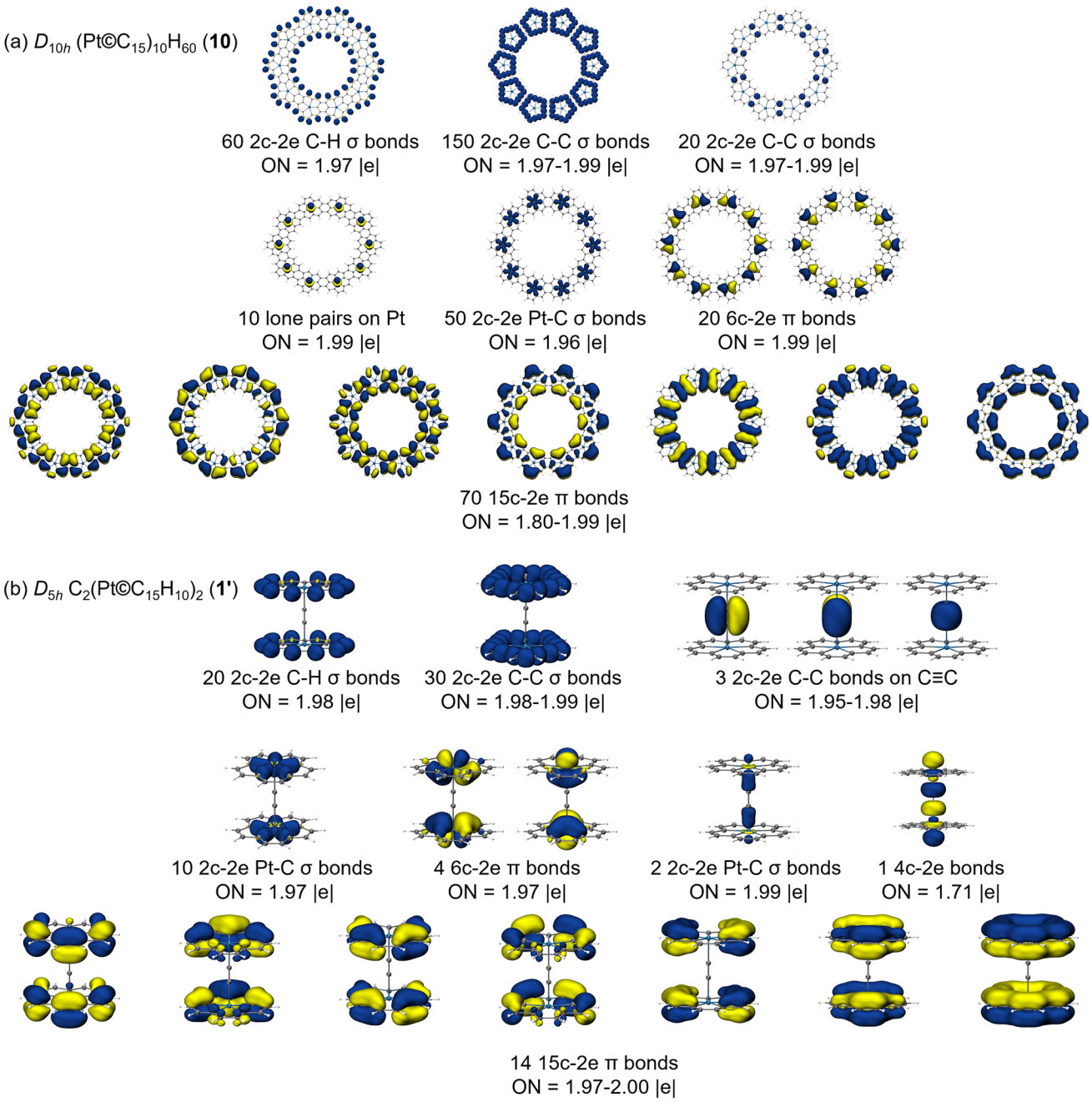

Fig. 5 AdNDP bonding pattern of (**a**) D_{10h} $(Pt©C_{15})_{10}H_{60}$ (**10**) and (**b**) D_{5h} $C_2(Pt©C_{15}H_{10})_2$ (**1'**), with the ON values indicated

Simulated IR, NMR, and UV–Vis spectra

Figure 6 exemplifies the simulated IR, Raman, and UV–Vis spectra of (a) D_{5h} $Pt©C_{15}H_{10}$ (**1**), (b) D_{5h} $C_2(Pt©C_{15}H_{10})_2$ (**1'**), (c) D_{2h} $(Pt©C_{15})_2H_{16}$ (**2**), and (d) D_{2h} $[C_2(Pt©C_{15})_2]_2H_{32}$ (**2'**) at B3LYP level. For $Pt©C_{15}H_{10}$ (**1**), four prominent IR peaks located at 502, 903, 1525, and 3140 cm^{-1} are assigned to aromatic ring vibration, C-H out-of-plane bending, conjugated C = C stretching and aromatic C-H stretching, respectively. Its five strong Raman signals at 335, 465, 1393, 1590, and 3143 cm^{-1} correspond to Pt-ligand skeleton vibration, ring breathing, aromatic C–C stretching, conjugated C = C skeleton vibration, and C-H stretching, respectively. The non-metal sandwich complex $C_2(Pt©C_{15}H_{10})_2$ (**1'**) shows four distinct IR absorption peaks at 393, 895, 1268, and 3126 cm^{-1}, which are attributed to Pt-ligand framework vibration, C-H out-of-plane bending, skeleton C–C stretching and C-H stretching. Its five Raman peaks at 146, 457, 1385, 1579, and 3128 cm^{-1} are attributed to low-frequency framework vibration, ring breathing, aromatic C–C/C = C

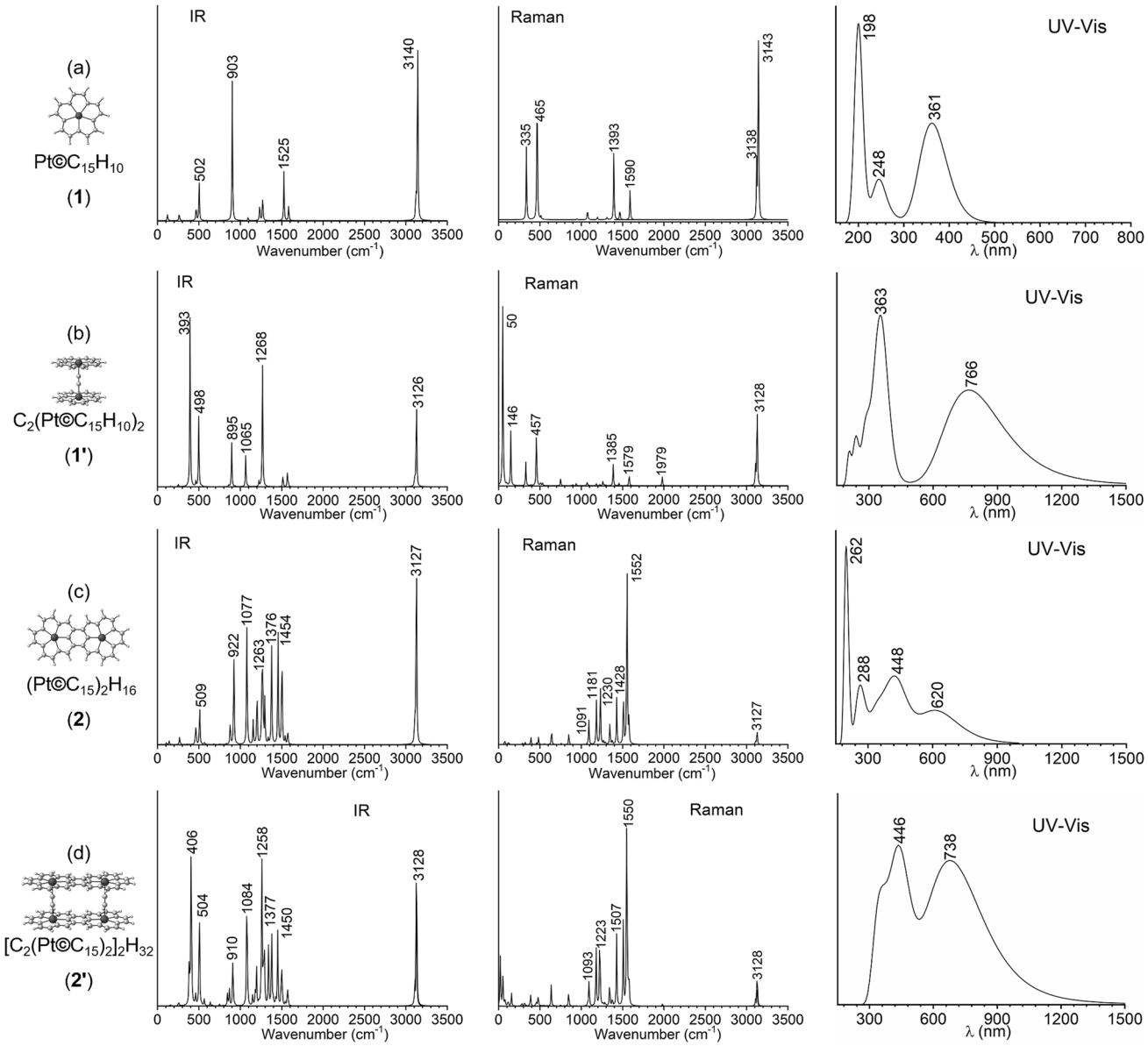

Fig. 6 Simulated IR, Raman and UV–Vis spectra of (a) D_{5h} $Pt©C_{15}H_{10}$ (**1**), (b) D_{5h} $C_2(Pt©C_{15}H_{10})_2$ (**1'**), (c) D_{2h} $(Pt©C_{15})_2H_{16}$ (**2**) and (d) D_{2h} $[C_2(Pt©C_{15})_2]_2H_{32}$ (**2'**) at B3LYP level

stretching and terminal C-H stretching modes. For planar $(Pt©C_{15})_2H_{16}$ (**2**), the dominant IR absorption at 509, 922, 1077, and 3127 cm^{-1} belong to cyclic skeleton bending, C-H out-of-plane bending, in-plane C-H stretching, while its characteristic Raman vibration at 1091, 1181, 1428, 1552, and 3127 cm^{-1} are assigned to aromatic in-plane bending, C–C and conjugated C = C stretching. The non-metal sandwich complex $[C_2(Pt©C_{15})_2]_2H_{32}$ (**2'**) displays four strong IR absorptions at 406, 910, 1258, and 3128 cm^{-1} and five Raman vibrations at 1093, 1223, 1507, 1550, and 3128 cm^{-1} follow similar vibrational behaviors, mainly involving metal-skeleton motion, aromatic ring bending, C–C/C = C stretching and C-H stretching vibrations. The simulated UV–Vis absorption spectra of these four complexes are dominated by singlet $\pi \rightarrow \pi^*$ electronic transitions. The $Pt©C_{15}H_{10}$ (**1**) exhibits major absorption bands at 361 nm and 198 nm. The $C_2(Pt©C_{15}H_{10})_2$ (**1'**) and $(Pt©C_{15})_2H_{16}$ (**2**) show new low-energy absorption peaks at 766 nm and 620 nm, respectively, while the $[C_2(Pt©C_{15})_2]_2H_{32}$ (**2'**) sandwich derivative presents the most red-shifted low-wavelength absorption at 738 nm. All main characteristic absorption peaks originate from frontier orbital electron transitions of the conjugated aromatic skeletons, and the continuous extension of the π-conjugated system effectively reduces the energy gap and broadens the light absorption range.

Conclusions

Extensive first-principle theory calculations and analyses performed in this work predict a series of stable [55555] metallo-annulene polymers $(Pt©C_{15})_nH_{6n+4}$ ($n = 2–9$) (**2–9**) and $(Pt©C_{15}H_6)_{10}$ (**10**), nonmetal bis([55555] metallo-annulene) sandwich complexes $C_2(Pt©C_{15}H_{10})_2$ (**1′**), $[C_2(Pt©C_{15})_2]_nH_{2(6n+4)}$ ($n = 2–9$) (**2′-9′**), and $[C_2(Pt©C_{15}H_6)_2]_{10}$ (**10′**), and tubular [55555] metallo-annulene nanobelts $(Pt©C_{15}H_6CH_2)_n$ ($n = 8$, 10, 12) (**11**, **12**, **13**) which are all composed of conjugated π-aromatic $Pt©C_{15}$ building blocks on the molecular frameworks. The metal-centered [55555] metallo-annulene sandwich-like D_{5h} $Cr_5(M©C_{40}H_{15})_2$ (**14'**) represent the first annulene sandwich complexes which contain both in-plane (Au, Ag, Cu) and out-of-plane (Cr) transition metal coordination centers, while the D_{nh} $(Pt©C_{15}H_6CH_2)_n$ ($n = 8$, 10, 12) (**11, 12, 13**) nanobelts may be extended in one-dimension to form 1D [55555] metallo-annulene nanotubes. Experimental syntheses and characterizations of such novel species starting from the right cycloaddition precursors [1] under suitable conditions would effectively enrich the chemistry and materials science of annulene complexes.

Supplementary Information The online version contains supplementary material available at https://doi.org/10.1007/s00894-026-06879-1.

Author contribution S.-D. Li and Q. Chen conceived the concepts and finalize the manuscript. X.-N. Zhao and Q.-W. Zhang performed the calculations and prepared the first draft.

Funding This work was financially supported by the National Natural Science Foundation of China (22373061 and 21973057 to S. D. L).

Data Availability No datasets were generated or analysed during the current study.

References

1. Xu B, Chen D, Ruan K et al (2025) Metal-centred planar [15] annulenes. Nature 641:106–111. https://doi.org/10.1038/s41586-025-08841-2
2. Astruc D (2023) The numerous paths of ferrocene. Nat Chem 15:1650. https://doi.org/10.1038/s41557-023-01348-1
3. Pampaloni G (2010) Aromatic hydrocarbons as ligands. Recent advances in the synthesis, the reactivity and the applications of bis(η^6-arene) complexes. Coord Chem Rev 254:402–419. https://doi.org/10.1016/j.ccr.2009.05.014
4. Jacoby M (2025) Ring around the osmium. C&EN Global Enterprise 103(12):6–7. https://doi.org/10.1021/cen-10312-scicon3
5. Zhao XN, Wei JF, Chen Q, Li SD (2025) Prediction of perfect aromatic in-plane [55555] metallo-annulenes. Eur J Inorg Chem 28:e202500420. https://doi.org/10.1002/ejic.202500420
6. Stephens PJ, Devlin FJ, Chabalowski CF, Frisch MJ (1994) Ab initio calculation of vibrational absorption and circular dichroism spectra using density functional force fields. J Phys Chem 98:11623–11627. https://doi.org/10.1021/j100096a001
7. Lee C, Weitao Y, Parr RG (1988) Development of the Colic-Salvetti correlation-energy formula into a functional of the electron density. Phys Rev B 37:785. https://doi.org/10.1103/PhysRevB.37.785
8. Frisch MJ, Trucks GW, Schlegel HB, et al (2009) Gaussian 09, Revision A.1, Gaussian Inc
9. Andrae D, Häußermann U, Dolg M et al (1990) Energy-adjustedab initio pseudopotentials for the second and third row transition elements. Theor Chim Acta 77:123–141. https://doi.org/10.1007/BF01114537
10. Hehre WJ, Ditchfield R, Pople JA (1972) Self-consistent molecular orbital methods. XII. Further extensions of Gaussian-type basis sets for use in molecular-orbital studies of organic molecules. J Chem Phys 56:2257–2261. https://doi.org/10.1063/1.1677527
11. Hariharan PC, Pople JA (1973) Influence of Polarization Functions on Molecular-Orbital Hydrogenation Energies. Theoretica Chimica Acta 28:213–222. https://doi.org/10.1007/BF00533485
12. Casida ME, Jamorski C, Casida KC, Salahub DR (1998) Molecular excitation energies to high-lying bound states from time-dependent density-functional response theory: characterization and correction of the time-dependent local density approximation ionization threshold. J Chem Phys 108:4439–4449. https://doi.org/10.1063/1.475855
13. Bauernschmitt R, Ahlrichs R (1996) Treatment of electronic excitations within the adiabatic approximation of time dependent density functional theory. Chem Phys Lett 256:454–464. https://doi.org/10.1016/0009-2614(96)00440-X
14. Marenich AV, Cramer CJ, Truhlar DG (2009) Universal solvation model based on solute electron density and on a continuum model of the solvent defined by the bulk dielectric constant and atomic surface tensions. J Phys Chem B 113:6378–6396. https://doi.org/10.1021/jp810292n
15. VandeVondele J, Hutter J (2007) Gaussian basis sets for accurate calculations on molecular systems in gas and condensed phases. J Chem Phys 127:114105. https://doi.org/10.1063/1.2770708
16. Kühne TD, Iannuzzi M, Del Ben M et al (2020) CP2K: An electronic structure and molecular dynamics software package -Quickstep: Efficient and accurate electronic structure calculations. J Chem Phys 152:194103–194149. https://doi.org/10.1063/5.0007045
17. Perdew JP, Burke K, Ernzerhof M (1996) Generalized gradient approximation made simple. Phys Rev Lett 77:3865–3868. https://doi.org/10.1103/PhysRevLett.77.3865
18. Zubarev DY, Boldyrev AI (2008) Developing paradigms of chemical bonding: adaptive natural density partitioning. Phys Chem Chem Phys 10:5207–5217. https://doi.org/10.1039/b804083d
19. Tkachenko NV, Boldyrev AI (2019) Chemical bonding analysis of excited states using the adaptive natural density partitioning method. Phys Chem Chem Phys 21:9590–9596. https://doi.org/10.1039/c9cp00379g
20. Geuenich D, Hess K, Köhler F, Herges R (2005) Anisotropy of the induced current density (ACID), a general method to quantify and visualize electronic delocalization. Chem Rev 105:3758–3772
21. Herges R, Geuenich D (2001) Delocalization of electrons in molecules. J Phys Chem A 105:3214–3220. https://doi.org/10.1021/jp0034426
22. Fliegl H, Taubert S, Lehtonen O, Sundholm D (2011) The gauge including magnetically induced current method. Phys Chem Chem Phys 13:20500–20518. https://doi.org/10.1039/C1CP21812C
23. Humphrey W, Dalke A, Schulten K (1996) VMD: visual molecular dynamics. J Mol Graph 14:33–38. https://doi.org/10.1016/0263-7855(96)00018-5
24. (2020) CYLview20; Legault, C. Y., Université de Sherbrooke, 2020 (http://www.cylview.org)

25. Rodríguez-Rubio A, Zhu H, Man Cheung K et al (2025) Synthesis of triple stranded porphyrin nanobelts. Science 390:290–293. https://doi.org/10.1126/science.adz8900